Interferences and asymmetries in laser-assisted photoionization of diatomic molecules

Diego I. R. Boll and Omar A. Fojón*
Instituto de Física Rosario, CONICET-UNR, Blvd. 27 de Febrero 210 bis, 2000 Rosario, Argentina
(Received 20 August 2014; published 12 November 2014)

Several kinds of interference effects in laser-assisted photoionization of H_2^+ molecular targets are theoretically investigated by means of a Coulomb-Volkov model. The photoelectron angular distributions in the single-photon ionization reaction are compared to more elaborated results, and the influence of usual approximations are studied. Several configurations of pulses and assistant lasers are considered. Moreover, we show that previous interference effects predicted for monochromatic pulses could be enhanced and/or diminished leading to a directional selectivity of photoelectron emission. Finally, we analyze the influence of the pulse duration on the photoelectron spectrum.

DOI: 10.1103/PhysRevA.90.053414 PACS number(s): 33.20.Xx, 33.60.+q

I. INTRODUCTION

The development of the attosecond (as, 1 as $= 10^{-18}$ s) science has opened the possibility to explore the electron dynamics in its own space and time scale. In this context, it has also the potential of bringing promising tools able to manipulate the electron dynamics, as the first step towards the goal of controlling chemical reactions by a direct action on their fundamental constituents. Many different techniques have been developed to reach this goal. By using femtosecond (fs, 1 fs $= 10^{-15}$ s) technology, it has been possible to control chemical reactions at the nuclear motion time scale, demonstrating that the breaking of a given molecular bond was an achievable process [1]. A few years later, the development of ultrashort light sources has pushed the time resolution from several hundreds of attoseconds [2] to less than one hundred attoseconds [3], i.e., close to the electronic motion time scale in atoms or molecules. Concepts such as control of the electron dynamics in a reaction emerged as a consequence of those technological achievements. Moreover, the ionization of a coherent superposition of states [4,5], the control of electron localization in dissociating molecular states [6–9], and, recently, the control of orbital parity mix [10] have been proved to be valid tools to control dynamical properties in reactions. The key ingredient in all those works is the different types of interferences that arise, particularly those generating asymmetric distributions of fragments of the reaction. When considered in conjunction with the Young-like (see [11] and references therein) and confinement [12,13] interferences, a wider range of effects are expected to emerge. Moreover, interferences can arise due to differences in the phase shift of the wave packets released by the several pulses composing the ionizing signal [14–16].

The generation of single attosecond pulses (SATP) or attosecond pulse trains (ATPTs) is usually achieved through high harmonic generation by focusing an intense ultrashort infrared laser pulse into a noble gas atom chamber [17]. The characterization of SATPs and ATPTs has been studied both theoretically and experimentally [18,19]. The widespread experimental procedure is the conversion of these light bursts in electron wave packets photoionizing atoms in the presence of a near-infrared laser field (NIR).

The theoretical approach to the problem is by no means simpler. Solving the time-dependent Schrödinger equation for reactions such as the photoionization of molecular targets assisted by a NIR laser represents a computational challenge [20–23], and also numerical results normally do not have a straightforward interpretation. The use of simplified models leading to predictions in reasonable agreement with *ab initio* calculations could be a valuable tool to understand the physical processes involved. The strong-field approximation (SFA) was one of the first available models to tackle these problems. Within this approximation, the Coulomb interaction between the residual target and the photoelectron is not taken into account in the dynamics of the latter one [24]. Nowadays, more elaborated models are available. Among them, the separable Coulomb-Volkov (SCV) model deals with atomic or molecular targets [25–27] including the Coulomb interaction in the final channel of the reaction. In the SCV approach, there are three time steps in the electronic evolution. In the first one, the ionized electron evolves as if it were subject exclusively to the Coulomb field of the target, whereas in the third and last interval of time, photoelectrons are described by the Volkov continuum irrespective of the relative importance of Coulomb and laser fields [26]. In the intermediate step, both the Coulomb and NIR laser fields are acting on the ejected electron and are of comparable importance. It is worth mentioning that the SCV for the case of simple molecular targets described by linear combination of atomic orbitals (LCAO) leads to analytical expressions simplifying the computation of the observables for the reaction.

In this work, we show that the SCV model gives a qualitative agreement with *ab initio* calculations of monochromatic photoionization cross sections [12,13,28] of H_2^+ molecules. Then, we analyze the case where the reaction is initiated by a SATP or an ATPT assisted by a NIR laser in the so-called streaking regime [16], focusing on those conditions where asymmetrical fragments (i.e., photoelectron signals) are generated. Different pulse durations ranging from 100 as to 2.5 fs and three possible polarizations are considered. The initial molecular wave functions are described here as a linear combination of Slater-type orbitals (STOs) variationally optimized, whereas the final wave functions are SCV-type wave functions [26]. Employing these initial and final wave

*Escuela de Ciencias Exactas y Naturales, Universidad Nacional de Rosario, Argentina.

functions, analytical expressions for the observables of interest, such as photoionization spectra and photoelectron angular distributions (PADs), are obtained.

Atomic units are used if not otherwise explicitly stated.

II. THEORY

Let us consider the photoionization of a diatomic molecule through an ATPT assisted by a monochromatic NIR laser. To fix ideas, we consider the case of the H_2^+ target as its theoretical description is simpler than other multielectronic molecules. In the following, we summarize the basic ingredients of the SCV model [26].

The coordinate system used is one where $\mathbf{R}$ is the internuclear vector pointing from nuclei 1 to 2 and $\mathbf{r}_i$ denotes the electron position vector with respect to the ith nuclei. The electron coordinate with respect to the molecular center of mass will be given by $\mathbf{r} = (\mathbf{r}_1 + \mathbf{r}_2)/2$.

The matrix transition amplitude in the dipole approximation corresponding to the photoionization reaction by an ATPT in the extreme ultraviolet regime (XUV) in the presence of a NIR laser bath is given in the velocity gauge by [24]

$$M_{\mathrm{SCV}}(\mathbf{p}) = -i \int_{-\infty}^{\infty} dt \langle \Psi_f(\mathbf{r},t) | \hat{\mathbf{p}} \cdot \mathbf{A}(t) | \Psi_i(\mathbf{r},t) \rangle, \quad (1)$$

where $\hat{\mathbf{p}}$ is the momentum operator, and $\Psi_i(\mathbf{r},t)$ and $\Psi_f(\mathbf{r},t)$ are the initial and final wave functions corresponding to the initial and final channels of the reaction, respectively.

The vector potential $\mathbf{A}(t)$ representing the XUV pulse is given by

$$\mathbf{A}(t) = \mathbf{\Pi}(\phi) A_0 \sum_k \varsigma_k e^{-i\Omega t} \exp\left[-\frac{(t-t_k)^2}{2\tau^2} \right], \quad (2)$$

$$= \mathbf{\Pi}(\phi) A_0 \tau \sqrt{\frac{1}{2\pi}} \int_{-\infty}^{\infty} R(\omega) e^{-i(\omega+\Omega)t} d\omega, \quad (3)$$

where Ω is the central frequency of the attosecond pulse. $\mathbf{\Pi}(\phi)$ and A_0 represent the polarization vector and the amplitude of each pulse in the ATPT, respectively. The duration of the attopulses denoted by τ is related to its full width at half maximum (FWHM) duration through $\tau_{\mathrm{FWHM}} = 2\sqrt{\ln 2}\tau$. The interference factor represented by $R(\omega)$ in Eq. (3) is given by

$$R(\omega) = \sum_k \varsigma_k \exp[i\omega t_k - \omega^2 \tau^2/2], \quad (4)$$

where t_k is the arrival time of the k-esime pulse composing the ATPT and ς_k is a factor that can assume the values ± 1 according to the kind of simulated ATPT.

For low and intermediate NIR laser intensities ($I_L < 10^{13}$ W/cm^2), one can reasonably approximate the bound initial states by *laser-free* wave functions, i.e.,

$$\Psi_i(\mathbf{r},t) = \psi_i^0(\mathbf{r}) \exp(i I_p t), \quad (5)$$

where I_p is the ionization potential of the initial molecular bound state given by ψ_i^0. The *laser-free* approximation is justified for the NIR intensities of interest in our work as in [29]. This is in agreement also with a large value of the Keldysh parameter γ ($\gamma \sim 9$ in our case), indicating that the NIR laser field does not induce important modifications to the Coulomb potential, i.e., the NIR may ionize the target only by a multiphoton ionization, a process which is unlikely to occur with the considered NIR intensities.

The initial molecular bound state is represented by a two center development in terms of Slater-type functions located on each molecular center (labeled as 1 and 2),

$$\psi_i^0(\mathbf{r}) = \sum_j c_j^{(1)} \phi_j(\mathbf{r}_1) + \sum_k c_k^{(2)} \phi_k(\mathbf{r}_2), \quad (6)$$

where $\phi_i(\mathbf{r})$ are STOs.

We describe the asymptotic final states of the electron by the Coulomb-Volkov *ansatz* [26] in which the interaction of the ejected electron with both the residual ionic target and the laser bath is taken into account,

$$\Psi_f(\mathbf{r},t) = \psi_f^0(\mathbf{r}) \exp\left\{ -\frac{i}{2} \int^t [\mathbf{p} + \mathbf{A}_L(t')]^2 dt' \right\}, \quad (7)$$

with $\mathbf{p}$ the asymptotic value of the photoelectron momentum and $\mathbf{A}_L(t)$ the potential vector describing the NIR laser field. The wave function $\psi_f^0(\mathbf{r})$ describes the continuum states of the molecule [25], being given by

$$\psi_f^0(\mathbf{r}) = (2\pi)^{-3/2} e^{i\mathbf{p}\cdot\mathbf{r}} N_p^2 G(\mathbf{r}_1) G(\mathbf{r}_2), \quad (8)$$

where $N_p = \Gamma(1 + i\nu) \exp(\pi\nu/2)$ and $G(\mathbf{r}_i) = {}_1F_1(-i\nu_i; 1; -i(pr_i + \mathbf{p}\cdot\mathbf{r}_i))$ is the confluent hypergeometric function, and the Sommerfeld parameter is $\nu_i = Z_i/p$, where Z_i is the residual effective charge of the i-esime atom.

The phase multiplying the $\psi_f^0(\mathbf{r})$ wave function in Eq. (7) is the well-known Volkov phase describing an electron of momentum $\mathbf{p}$ in the presence of an electromagnetic field represented by the potential vector $\mathbf{A}_L$ in our case. This vector potential corresponds to the NIR laser field and is given by

$$\mathbf{A}_L(t) \cong -\frac{\mathbf{E}_1}{\omega_0} \sin(\omega_0 t) - \frac{\mathbf{E}_2}{\omega_0} \sin(\omega_0 t + \phi_L), \quad (9)$$

where ω_0 is the laser field frequency corresponding to the mutually perpendicular electric field components $\mathbf{E}_{1,2}$, respectively, and ϕ_L is an arbitrary phase. The respective electric field is given thus by

$$\mathbf{E}_L(t) = -\frac{d\mathbf{A}_L}{dt} \approx \mathbf{E}_1 \cos(\omega_0 t) + \mathbf{E}_2 \cos(\omega_0 t + \phi_L). \quad (10)$$

Replacing Eqs. (3), (5), (7), and (9) into Eq. (1), recognizing that in the velocity gauge, time and space integrals are separable, and making use of the Jacobi-Anger development [26,27] to expand the time-dependent terms in the Volkov phase, the matrix transition amplitude given by Eq. (1) may be rewritten as

$$M_{\mathrm{SCV}}(\mathbf{p}) = A_0 \tau \sqrt{2\pi}\, M_{\mathrm{ph}}(\mathbf{p}) \sum_{m_{1,2}, n_{1,2} = -\infty}^{\infty} i^{n_1+n_2} (-1)^{m_1+m_2} \times R(\omega) J_{m_1}(M_1) J_{m_2}(M_2) J_{n_1}(N_1) J_{n_2}(N_2) \times e^{i(2m_2+n_2)\phi_L}, \quad (11)$$

where we have defined

$$M_{1,2} = E_{1,2}^2/(2\omega_0)^3, \quad (12)$$

$$N_{1,2} = \mathbf{p}\cdot\mathbf{E}_{1,2}/\omega_0^2, \quad (13)$$

$$\omega = p^2/2 + I_p - \Omega + (2M_1 + 2m_1 + n_1)\omega_0 + (2M_2 + 2m_2 + n_2)\omega_0. \quad (14)$$

It is worth mentioning that the quadruple sum in Eq. (11) collapses to a double sum in m_1 and n_1 or m_2 and n_2 when $E_1 = 0$ or $E_2 = 0$, respectively, i.e., when considering a NIR with just one component.

The monochromatic transition matrix element $M_{\rm ph}(\mathbf{p})$ is given by

$$M_{\rm ph}(\mathbf{p}) = -i\langle\psi_f^0(\mathbf{r})|\mathbf{\Pi}(\phi)\cdot\nabla|\psi_i^0(\mathbf{r})\rangle. \quad (15)$$

To obtain $M_{ph}(\mathbf{p})$, we employ the Coulomb continuum (CC) model [25,26] in which a peaking approximation, summarized in the Appendix, is performed. This approximation, valid when $pR \gg 1$ leads to the following expression,

$$M_{\rm ph}(\mathbf{p}) = \chi_1 M_{\rm at}^{(1)} + \chi_2 M_{\rm at}^{(2)}, \quad (16)$$

where the molecular interference factors denoted by $\chi_{1,2}$ are given by

$$\chi_{1,2} = N_p^* e^{\pm i\mathbf{p}\cdot\mathbf{R}/2} G^*(\mp\mathbf{R}), \quad (17)$$

and the $M_{\rm at}^{(1,2)}$ factors correspond to the atomic transition matrix amplitudes from the molecular centers 1 and 2, respectively.

Therefore, the photoelectron spectrum is given by

$$\frac{d^3P_{\rm SCV}}{dp\,d\Omega_e} \equiv S(p,\theta_e,\phi_e) = p^2|M_{\rm SCV}(\mathbf{p})|^2, \quad (18)$$

where $d\Omega_e = \sin\theta_e d\theta_e d\phi_e$ denotes the differential solid angle in the direction of the asymptotic momentum of the photoelectron.

III. RESULTS

First, we compare our SCV results with more elaborated ones [21–23]. We test our monochromatic transition amplitude by computing photoelectron angular distributions (PADs) for H_2^+ targets with a definite spatial orientation and a XUV pulse with both polarization vector parallel and perpendicular with respect to the internuclear vector $\mathbf{R}$. Moreover, we include the case of circular polarization.

Second, we consider different configurations of XUV pulses and NIR in the streaking regime for two different XUV energies, analyzing the interferences produced by coherent emission from both nuclei and those generated by the presence of the NIR. We also include a study of the photoelectron spectrum dependence with SATPs or ATPTs individual pulse durations, from 100 as and up to almost the NIR period (2.5 fs).

Finally, we consider the case where both SATP or ATPT and NIR have circular polarization, studying the angle-energy photoelectron spectrum.

A. Monochromatic PADs

In Fig. 1, we present our computed PADs for three different photon frequencies $\Omega = 5$, 9.5, and 16 a.u. for the above-mentioned polarization cases.

To obtain the initial molecular bound state, we use the GAMESS software package [30] at the restricted open-shell Hartree-Fock level of theory. A medium size $[4s2p1d]$ polarized basis set of atomic STOs [31] was used by means of a STO-6G expansion [32]. Choosing the internuclear distance

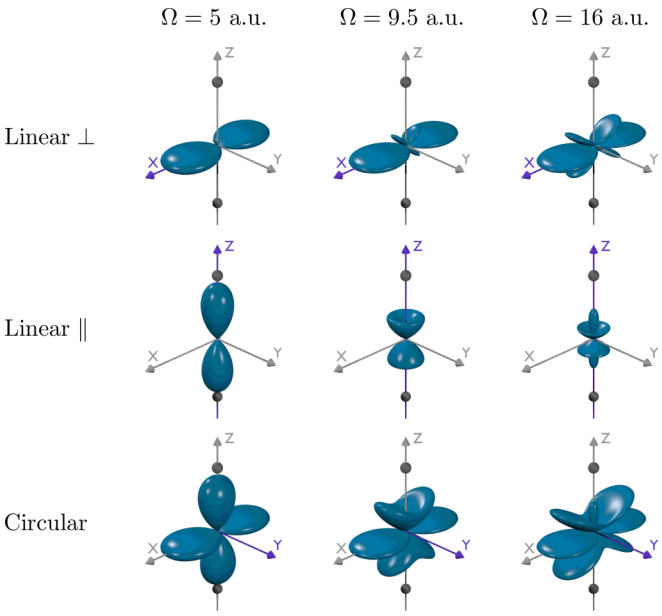

FIG. 1. (Color online) Monochromatic PADs (green-blue plots) for H_2^+ at $R = 2$ a.u., for XUV with linear polarization parallel and perpendicular to the molecular internuclear axis as well as circular polarization. The nuclei are indicated by two small spheres (dark gray). For linear polarization (upper and middle panels), the polarization vector is indicated by a purple axis. In the case of circular right polarization, the purple axis indicates the incidence direction.

equal to the equilibrium value $R = 2$ a.u. leads to an ionization potential $I_p = 1.1019$ a.u.

For linear perpendicular polarization, the presence of extra lobes in directions other than the one of the polarization reveals the existence of interferences that may be related to Young type two-slit patterns [12,22]. At the lowest-energy case, the wavelength of the photoelectrons is slightly greater than the internuclear separation and even in that case small extra lobes are present. As the photon energy increases, the PADs resemble the distribution in Young's two-slit experiment [21].

When the polarization is parallel to the molecular internuclear axis, a different scenario appears. In general, photoelectrons are ejected mainly in the classical direction given by the polarization vector. However, ejection in this direction is partially forbidden for $\Omega = 9.5$ a.u. This can be associated to the so-called confinement effect that appears when the energy of the ejected photoelectron approximately satisfies $pR \sim l\pi$, with l being an odd integer. Moreover, this confinement effect may be traced to the presence of a minimum in the cross sections as a function of the photon energy for the particular l partial wave contribution [12,13,22]. Alternatively, this may be understood also as a Cooper minima-type consequence [33].

In the case of circular polarization, our PADs exhibit roughly a mixture of both linear parallel and linear perpendicular cases with an additional feature given by a *torsion* [23] of the PADs. Setting the polarization vector $\mathbf{\Pi}(\phi) = \cos(\phi)\mathbf{e}_z + i\,\sin(\phi)\mathbf{e}_x$ with $\phi = +\pi/4(-\pi/4)$ we get left (right) circular polarization XUV pulses. All the calculations with circular polarization were performed by setting $\phi = -\pi/4$. Replacing the circular polarization expression into Eq. (15), monochromatic

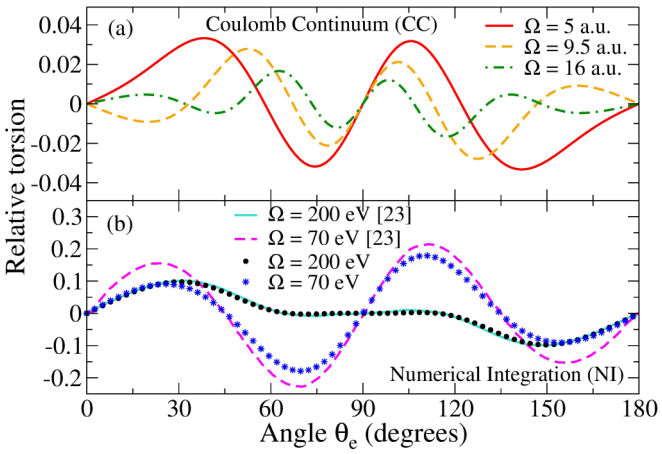

FIG. 2. (Color online) Relative torsion at different photon energies and right circular XUV polarization, in monochromatic photoionization of H_2^+ molecules at $R = 2$ a.u. Panel (a) shows the relative torsion obtained with CC model. Panel (b) shows relative torsion for numerical integration of Eq. (15) compared to *ab initio* results [23]. Results in full and dashed lines in panel (b) were taken from [23].

transition amplitudes may be written as

$$M_{\rm ph} = M^z_{\rm ph} + M^x_{\rm ph}. \tag{19}$$

The relative torsion (RT) is proportional to the cross product between ionization transition amplitudes of the two independent components of the XUV field divided by the maximum of the PAD [23], i.e.,

$$M_{\rm RT} \propto M^{x\,*}_{\rm ph} M^z_{\rm ph} + M^{z\,*}_{\rm ph} M^x_{\rm ph}, \tag{20}$$

and can be seen in Fig. 2. Panel (a) shows the RT obtained with the CC model. For the lower-energy case, this RT is about three times smaller than in the *ab initio* results [23], but the qualitative $\sin(2\theta_e)$ behavior is reproduced.

This feature is quite sensitive to the description of the molecular initial bound state and the final photoelectron wave function. The inclusion of d ($l = 2$) states in the description of the initial wave function plays a major qualitative role. They allow the reproduction of the qualitative behavior; otherwise, a $\sin(3\theta_e)$ dependence is obtained. This can be understood in terms of dipolar couplings between initial-state basis set elements and the continuum partial waves that dominate in a given energy region. At $\Omega = 5$ a.u., the linear perpendicular polarization cross section is dominated by $l = 3$ partial waves, whereas for linear parallel polarization they have a non-negligible contribution [28].

We have also checked that this RT disappears if only 1 s STOs are used in the description of the initial state in the CC model. Moreover, no asymmetry is observed if the Coulomb interaction between the photoelectron and the residual target is not taken into account in the final continuum wave function as it occurs in the SFA, irrespective of the basis set considered to describe the initial bound state.

Finally, this RT is also affected by the peaking approximation considered in our calculations. A numeric evaluation of matrix elements in Eq. (15), as those shown in panel (b) of Fig. 2 for photon energies of $\Omega = 70$ and 200 eV, respectively, yields a RT in better agreement with more elaborate results [23]. While for a photon energy of $\Omega = 200$ eV a remarkable agreement with results taken from [23] is found, the $\Omega = 70$ eV case shows an oscillation and peaks in qualitative agreement. This can be related to the fact that the final photoelectron wave function considered is asymptotically correct. The lower the energy of the photon, the worse the description of continuum states.

B. Photoelectron spectrum in the streaking regime

The relationship between the duration of each pulse in the ATPT (τ) and the period of the NIR ($T_{\rm NIR}$) establishes different physical situations for the reaction. When the NIR gives a negligible ionization probability of the target but it is able to exchange a noticeable momentum with photoelectrons released by a *short* ($\tau/T_{\rm NIR} \ll 1$) XUV pulse, we are in the so-called streaking regime [16]. Classical [16], semiclassical [14,15], and quantum [26,34] formulations are used to explain the features exhibited by a system under the streaking conditions.

In Fig. 3, we show the photoelectron spectra as a function of the XUV-NIR delay and the asymptotic kinetic energy of the photoelectrons, in the so-called parallel detection geometry ($\theta_e = 0$) (PDG+). We consider SATPs or ATPTs of energy $\Omega = 5$ a.u. and $\Omega = 9.5$ a.u. with a FWHM pulse duration of 200 as in the presence of a linearly polarized NIR of 800 nm with intensity $I_L = 3.5 \times 10^{12}$ W/cm^2.

As can be seen in Figs. 3(a)–3(d), the photoelectron spectra as a function of the XUV-NIR delay shows an oscillation with the same period as the NIR, irrespective of the XUV photon energy. Moreover, the amplitude (in energy) of this oscillation depends on both the NIR strength and the photoelectron momentum. This dependence may be explained classically [16].

If the Coulomb interaction of the photoelectron with the residual target is neglected, then the value of its asymptotic momentum is related to its *birth* time t_0 (arrival time of the XUV pulse) through the simple relation,

$$\mathbf{p} = \mathbf{p}_0 - \mathbf{A}_L(t_0), \tag{21}$$

where $\mathbf{p}_0 = \sqrt{2(\Omega - I_p)}$ represents the unshifted momentum that would acquire the ionized electron by absorption of an XUV photon in the absence of the NIR laser field [17]. In this approximation, it is assumed that the photoelectron is acted on instantaneously by the laser field provoking a *jarring* in its classical motion. Moreover, it is worth mentioning that the quantum effects of the confinement interferences can be traced in Figs. 3(a) and 3(b). For the later one, confinement effects [12] are produced and their influence is superimposed to the well-known decrease of the cross sections as the asymptotic photoelectron energy increases. On the other hand, the photoelectron spectrum in Fig. 3(a) exhibits a smaller decrease rate as compared to photoelectron spectrum in Fig. 3(b) owing to the absence of confinement. A similar analysis can be performed for Figs. 3(c) and 3(d).

If a train of XUV pulses instead of a single one is employed, a SPIDER-like attosecond spectrometer [14,15] is obtained and the situation changes dramatically as can be seen in Figs. 3(e) and 3(f), where structures appear in the

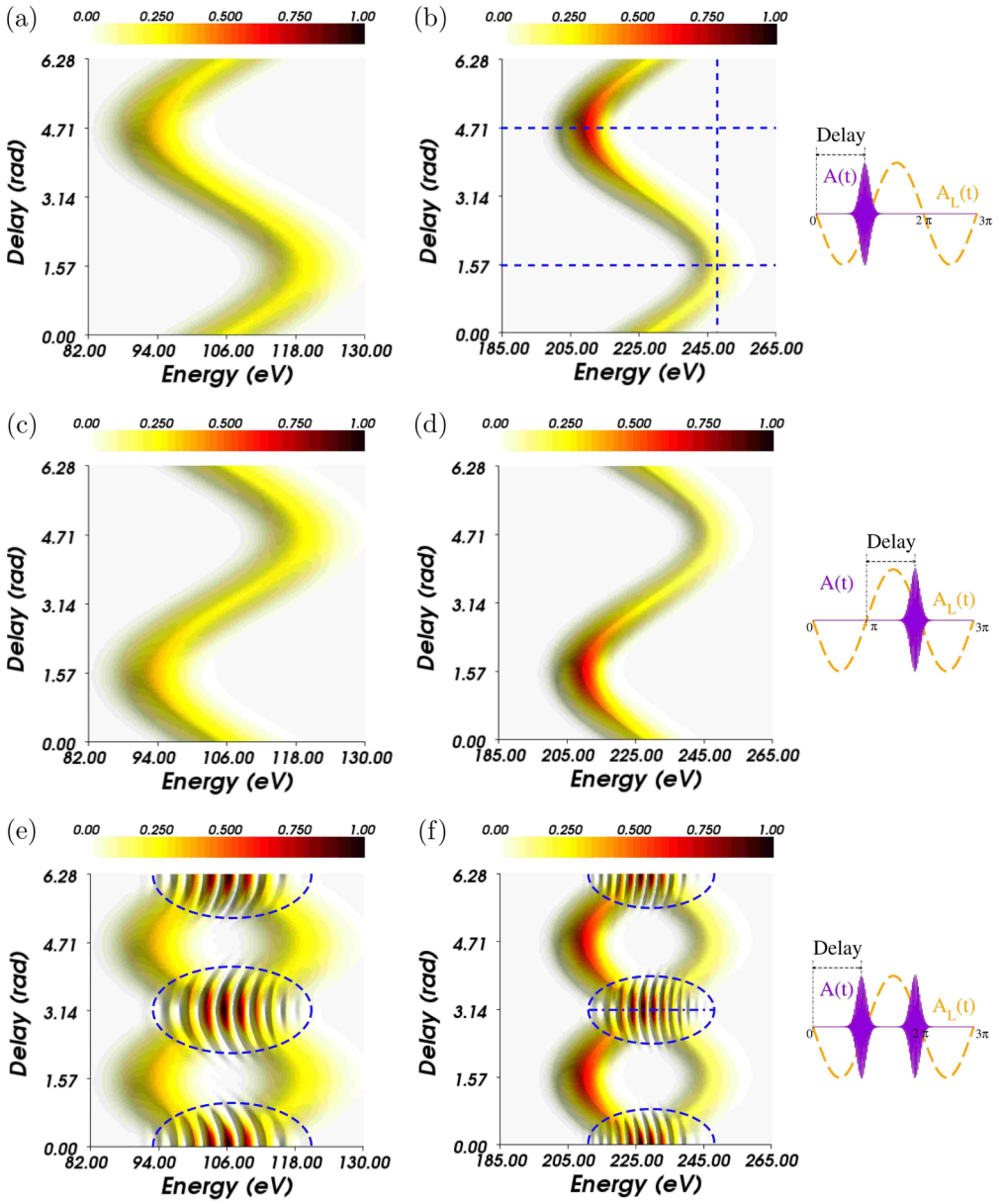

FIG. 3. (Color online) (a) Photoelectron spectrum in the PDG+ for H_2^+ at $R = 2$ a.u. ionized by a SATP of energy $\Omega = 5$ a.u. with a duration FWHM of 200 as, in the presence of a linearly parallel polarized NIR. The NIR wavelength and intensity are 800 nm and $I_L = 3.5 \times 10^{12}$ W/cm^2, respectively. (c) Same as (a) but with a SATP extra delay of π/ω_0. (e) Same as (a) but with an ATPT composed of a XUV pulse and a delayed replica. Figures (b), (d), and (f), the same as Figs. (a), (c), and (e), respectively, but XUV photon energy $\Omega = 9.5$ a.u. Sketches in the right-hand side show the delay definition schema.

crossing region, i.e., in the time-energy window delimited by dashed blue lines. These structures are a clear manifestation of quantum interferences produced by the existence of several quantum paths leading to the same final state [16].

Moreover, the relation between the bandwidth of the pulses in the ATPT and the intermediate NIR intensity regime considered gives rise to an interesting feature. The intensity is strong enough to impart a noticeable momentum transfer to the XUV released photoelectron, whereas the initial bound state remains almost unchanged [29]; also the bandwidth of the pulses is short enough to ensure that there will be regions where the energy gap cannot be overcome by absorption or emission of NIR photons. Under these conditions, two different behaviors coexist. Regions enclosed by dashed blue lines in the photoelectron spectrum of Fig. 3(e) present quantum mechanical features, i.e., interferences of photoelectron signals produced by each pulse in the ATPT, whereas the rest of the spectrum is almost equal to the incoherent superposition of the spectra generated by each of the two pulses comprising the ATPT. A similar behavior can be identified in Fig. 3(f) regardless of the confinement interference influence analyzed before. The dependence of this feature with the bandwidth of each pulse in the ATPT will be analyzed in the next section.

The existence of asymmetric emission patterns may be inferred from the energy-resolved photoelectron spectra, in the

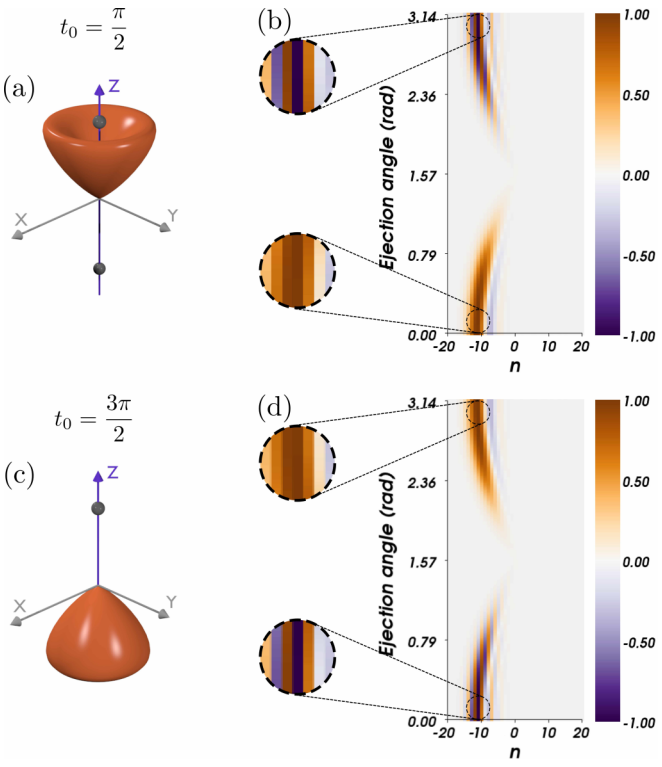

FIG. 4. (Color online) (a),(c) Laser-assisted PADs for H_2^+ at $R = 2$ a.u., with XUV polarization parallel to the molecular internuclear separation and different delays t_0. The polarization vector is indicated by a purple axis. Other parameters are the same as in Fig. 3(a). (b),(d) Interfering satellite terms in the quantum treatment (see text).

PDG+, shown in Figs. 3(a)–3(d). The photoelectrons emitted in the polarization direction have an energy that depends on the XUV-NIR delay t_0. Alternatively, the number of electrons with a given energy emitted in the PDG+ depends on the mentioned delay t_0. To further investigate these asymmetric emission patterns we computed the PADs with conditions corresponding to the crossings of the dashed blue lines in Fig. 3(b), i.e., $p^2/2 = 247$ eV and delays $t_0 = \pi/2\omega_0$ and $3\pi/2\omega_0$. They are shown in Figs. 4(a) and 4(c).

As can be seen, the presence of the NIR induce strong asymmetries compared to the completely symmetric case produced by the XUV solely [Fig. 1(e)].

Even if these asymmetries have been already found for assisted photoionization of atomic targets [14,15,34,35], the SCV model provides an interpretation of this effect based on interferences of the different channels opened by the NIR presence. Considering Eq. (11) with just one NIR component, we note that for the chosen NIR intensity the constant M_1 is close to zero ($M_1 = 0.067\,660\,152$), so $J_0(M_1) \gg J_{m_1}(M_1)$ with $m_1 \neq 0$. Thus the main contributions to the sum in Eq. (11) will be given by the partial sum in n_1 with $m_1 = 0$. We have also found that under these conditions the real and imaginary parts in this sum have a similar behavior, so it is only necessary to analyze one of them. In Figs. 4(b) and 4(d), we show the real part of the contributions of selected terms in the partial sum in n_1 with $m_1 = 0$. As can be seen, as the ejection angle approaches the value $\theta_e = \pi/2$, major contributions come from terms with a decreasing value of $|n|$. This may be related to the fact that momentum exchange between the photoelectron and NIR is proportional to $\mathbf{p}_0 \cdot \mathbf{A}_L(t_0)$ in the classical model [16,17], so when $\mathbf{p}_0 \perp \mathbf{A}_L$ there is no momentum exchange. In a quantum formulation, there will be no NIR photon absorption or emission by the photoelectron. More interesting is the observed upside-down asymmetry. In Fig. 4(b), for ejection angles θ_e belonging to $[0,\pi/2]$ almost all terms have a positive contribution to the sum, giving a nonvanishing upward probability of emission. On the contrary, for ejection angles θ_e in the domain $[\pi/2,\pi]$ the sign of the terms alternates between positive and negative, so different contributions to the partial sum cancel each other giving a negligible downward probability of emission, as can be seen in the colored zoomed areas. All these terms were previously identified as satellite interferences [26]. So we may conclude that the strong asymmetries shown in Figs. 4(a) and 4(c) come from interfering channels opened by the NIR. The results presented in Fig. 4(d) have a straightforward analogous interpretation.

As it has been shown in Figs. 3(e) and 3(f), when the ATPT is composed by two XUV pulses the spectra change in a marked fashion. The interferences in the crossing region come from the difference in the phase shift of the wave packets released by the pulses composing the ATPT [14–16].

In Fig. 5, we show the photoelectron spectrum for the PDG+ as a function of the asymptotic photoelectron energy corresponding to the dash-dotted blue line in Fig. 3(f). As can be seen, the signal is modulated in amplitude by a bell-shaped function. Moreover, it presents an oscillation of a slowly varying frequency. This spectrum can be accurately fitted with a function $f(E)$ given by

$$f(E) \propto (1 + \cos\gamma_n)|\mathcal{Z}_n|^2, \tag{22}$$

where the γ_n function is given in the Appendix, and the bell-shaped envelope is approximated in first ($n = 1$) and second

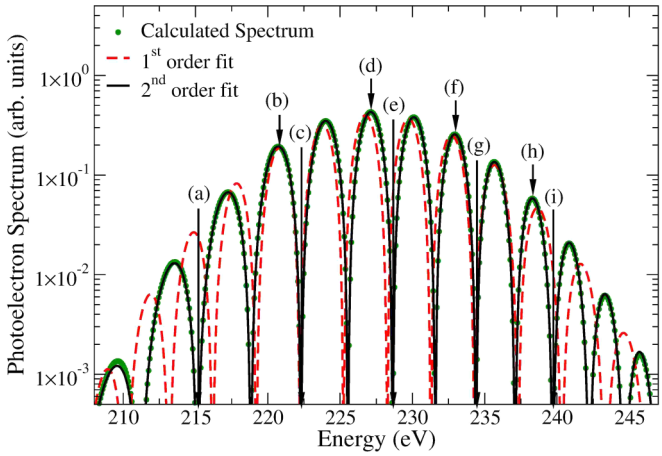

FIG. 5. (Color online) 2D cut of photoelectron spectrum in Fig. 3(f) for a delay between the ATPT and the NIR equal to $T_{\mathrm{NIR}}/2$. The calculated spectrum is given by the green small circles, whereas the fit with Eq. (22) is given by the continuous black line and dashed red line.

$(n = 2)$ order by

$$|\mathcal{Z}_1|^2 = \exp\left\{-a_1\tau^2\left(\frac{p^2}{2} - a_2\right)^2\right\}, \tag{23}$$

$$|\mathcal{Z}_2|^2 = \exp\left\{-a_1\tau^2\frac{\left(\frac{p^2}{2} - a_2\right)^2}{1 + p^2E_L^2\tau^4}\right\}, \tag{24}$$

where $a_{1,2}$ are considered as fitting free parameters.

It can be observed that the second-order fitting function provides reliable results all over the considered energy interval. On the other hand, the first-order fitting function is unable to reproduce accurately even the position of the central bands in the spectrum. This fact could be anticipated by means of the validity condition for a first-order fitting, given in Eq. (A27) of the Appendix. Replacing the corresponding values into Eq. (A27), we get $pE_L\tau^2 \sim 1$, where it is clear that the aforementioned condition is not met.

Interestingly, from this fitting procedure it may be possible to extract from γ_n the NIR intensity, the delay between XUV pulses, and the individual XUV pulse duration, the latter one appearing only in the second-order treatment $(n = 2)$.

For the energies indicated in Fig. 5 by letters and arrows, we have calculated the corresponding PADs that we present in Fig. 6 showing its variation with the asymptotic photoelectron energy for a fixed ATPT delay.

As can be seen, a small change in the asymptotic energy of the photoelectron has a deep influence on the PADs. The PAD closest to the central energy of the spectrum $(E = 8.4$ a.u.) is the one for $E = 228.681$ eV [indicated as (e) in Figs. 5 and 6]. PADs at both sides of the latter one show the same kind of behavior which ranges from almost complete erasure of the confinement effect [PAD (b) in Fig. 6] to an enhancement of this effect in one or both directions.

As expected, PADs corresponding to the various interference minima in Fig. 5 share a common feature, i.e., emission along the direction given by $\theta_e = 0$ vanishes, as can be seen in Figs. 6(a), 6(c), 6(e), 6(g), and 6(i). On the contrary, emission along $\theta_e = \pi$ is less regular. PADs far apart from the center energy of the spectrum [(a) and (i)] have a non-negligible probability in the $\theta_e = \pi$ direction, while the remaining PADs give an almost zero probability of emission in this direction.

Besides, the emergence of new structures in the PADs is clearly visible by comparing the monochromatic case [Fig. 1(e)] with the one closest to the central photoelectron energy. These structures comes from the fact that the action of the NIR opens several intermediate channels in the final one.

C. Photoelectron spectrum dependence with the ATPT pulse duration

The aim of this section is twofold. On one hand, we analyze the departures from the streakinglike behavior with an increasing pulse duration in the SATP. On the other hand, by changing the individual pulse duration in the SPIDER-like arrangement analyzed before, we study the influence of the pulse bandwidth on the spectrum.

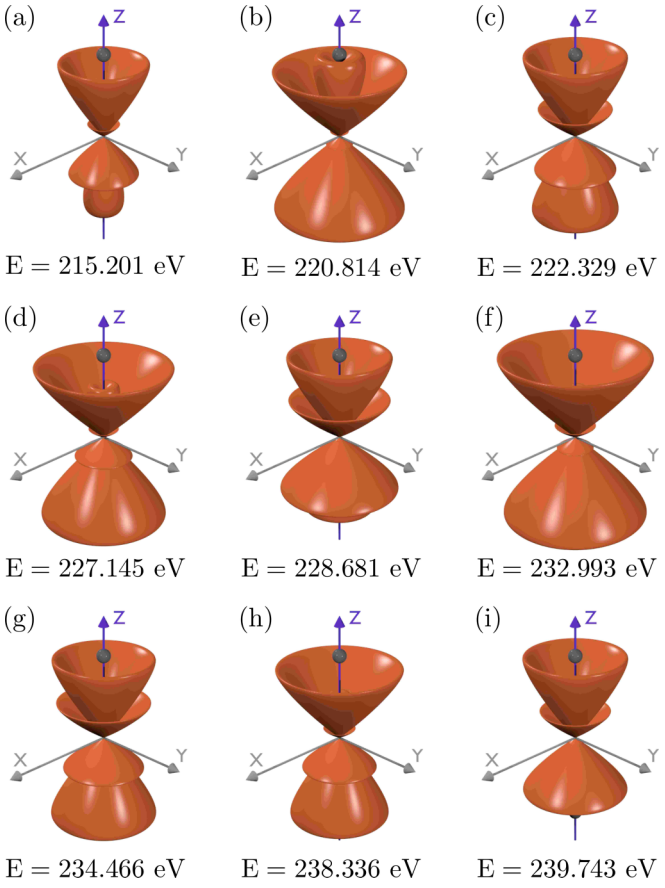

FIG. 6. (Color online) Angular distributions (orange plots) for several photoelectron asymptotic energies indicated in Fig. 5. All PADs were calculated for the same delay between the ATPT and the NIR. The rest of the parameters are the same as in Fig. 3(f).

As the pulse duration in the SATP increases, departures from the streaking regime behavior are observed owing to the interferences coming from the different quantum paths available. To study the dependence of the photoelectron spectrum with the pulse duration τ, we have computed this observable for different τ_{FWHM} values ranging from 100 as to 2.5 fs. In Fig. 7, a streakinglike behavior may be seen for pulse durations up to 500 as, where interferences arise for delays around $\pi/2\omega_0$ and $3\pi/2\omega_0$.

A subsequent increase of the pulse duration gives place to a rise in the number of sidebands and, at the same time, an erasing of the streakinglike behavior. Our calculated spectrum shows the same qualitative behavior as those of laser-assisted atomic photoionization [36]. However, in our case the presence of confinement interferences modifies the modulation in intensity of the sideband lines. For pulse durations reaching the period of the NIR, it is almost impossible to distinguish oscillations as a function of the delay showing that with increasing XUV pulse duration the spectrum becomes delay independent, as shown in the atomic case [36]. Moreover, the sidebands separation tends to the NIR photon energy, as the XUV pulse duration increases.

In Fig. 8, we focus on the case of an ATPT composed by two pulse replicas where some sort of sidebands appears even in the case of short durations. This may be ascribed to the

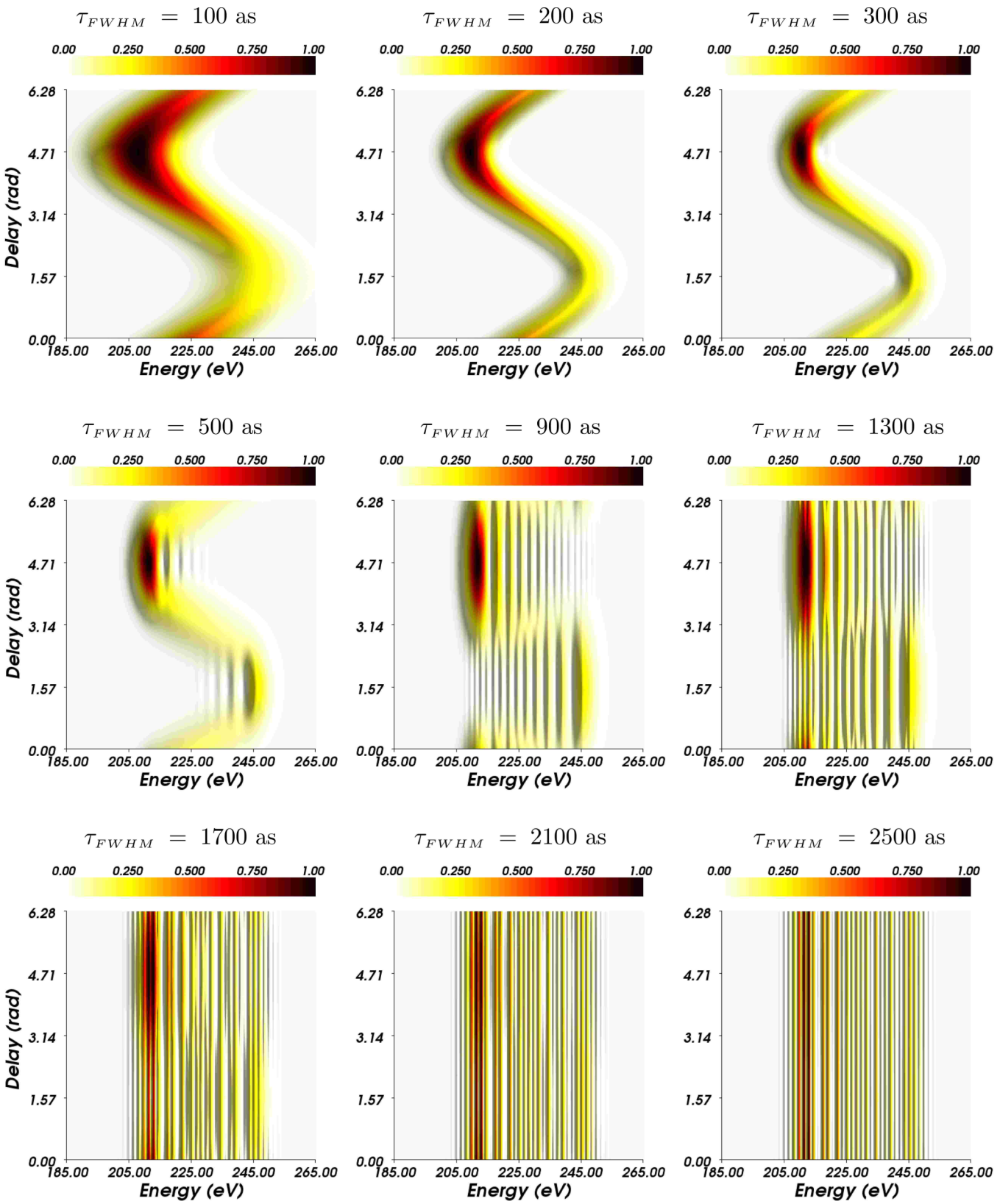

FIG. 7. (Color online) Photoelectron spectra for fixed in space H_2^+ at $R = 2$ a.u. for a linearly polarized SATP parallel to the molecular internuclear axis. The driven NIR is collinear to the SATP. Different pulse durations are considered. The other parameters are the same as in Fig. 3(f).

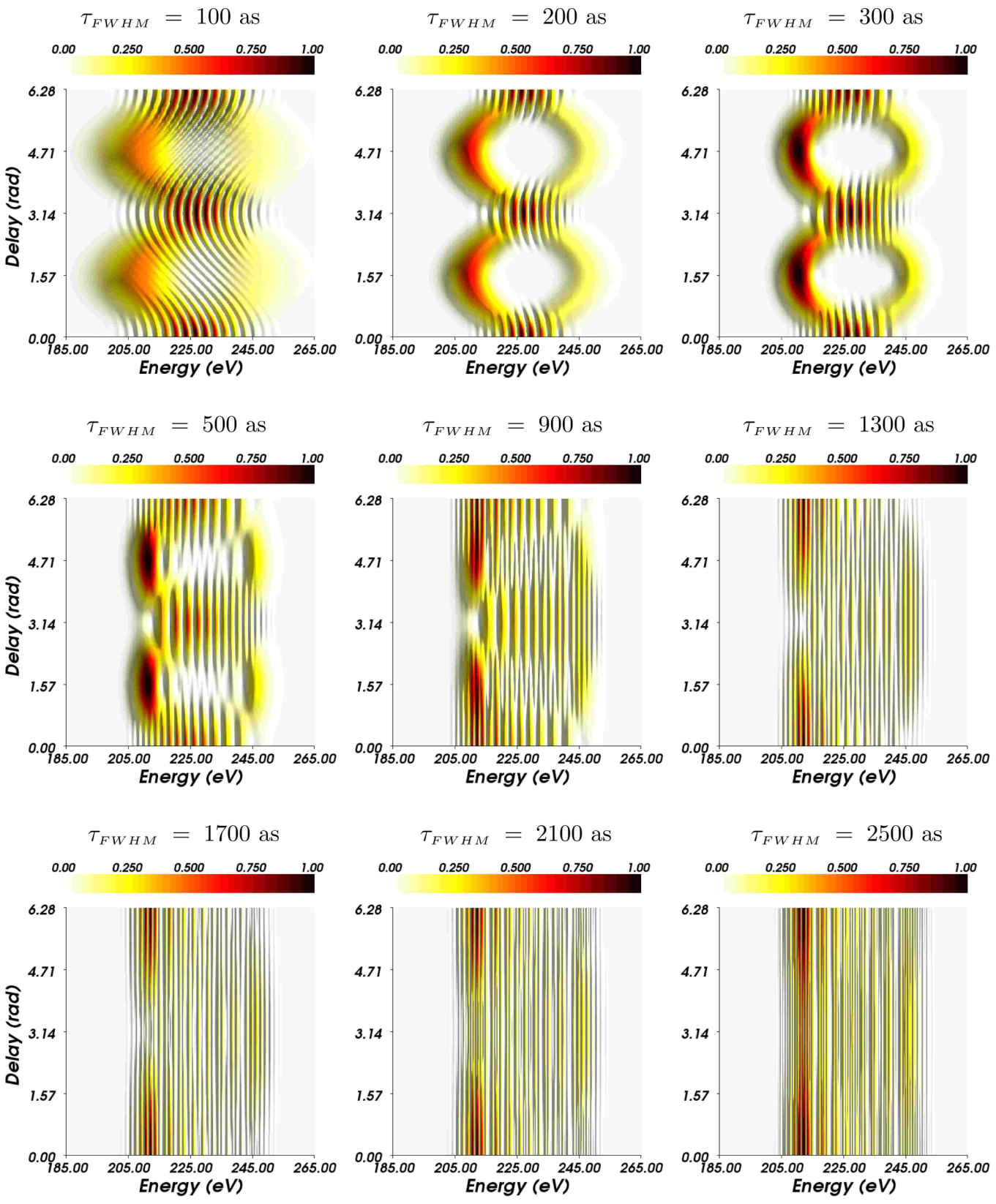

FIG. 8. (Color online) Same as Fig. 7 but for ionization with an ATPT composed by a pulse and a half NIR period delayed replica.

fact that for such a short duration of the pulses, the bandwidth broadening allows the formation of interferences produced by the signals generated by the two pulses comprising the ATPT and mediated by NIR photons. As long as the individual pulse duration increases, a hybrid coherent and incoherent superposition region behavior as the one analyzed in the previous section emerges at least up to $\tau_{\mathrm{FWHM}} = 500$ as, where sideband formations are almost all over the spectrum. For

longer pulse durations, the changes are of the same type as in the case of SATP, except that oscillations as a function of the delay are present even for the longest pulse duration considered, indicating that a dependence of the spectrum with the delay persists even if streakinglike features are not present. Under these conditions and opposed to what happens with a

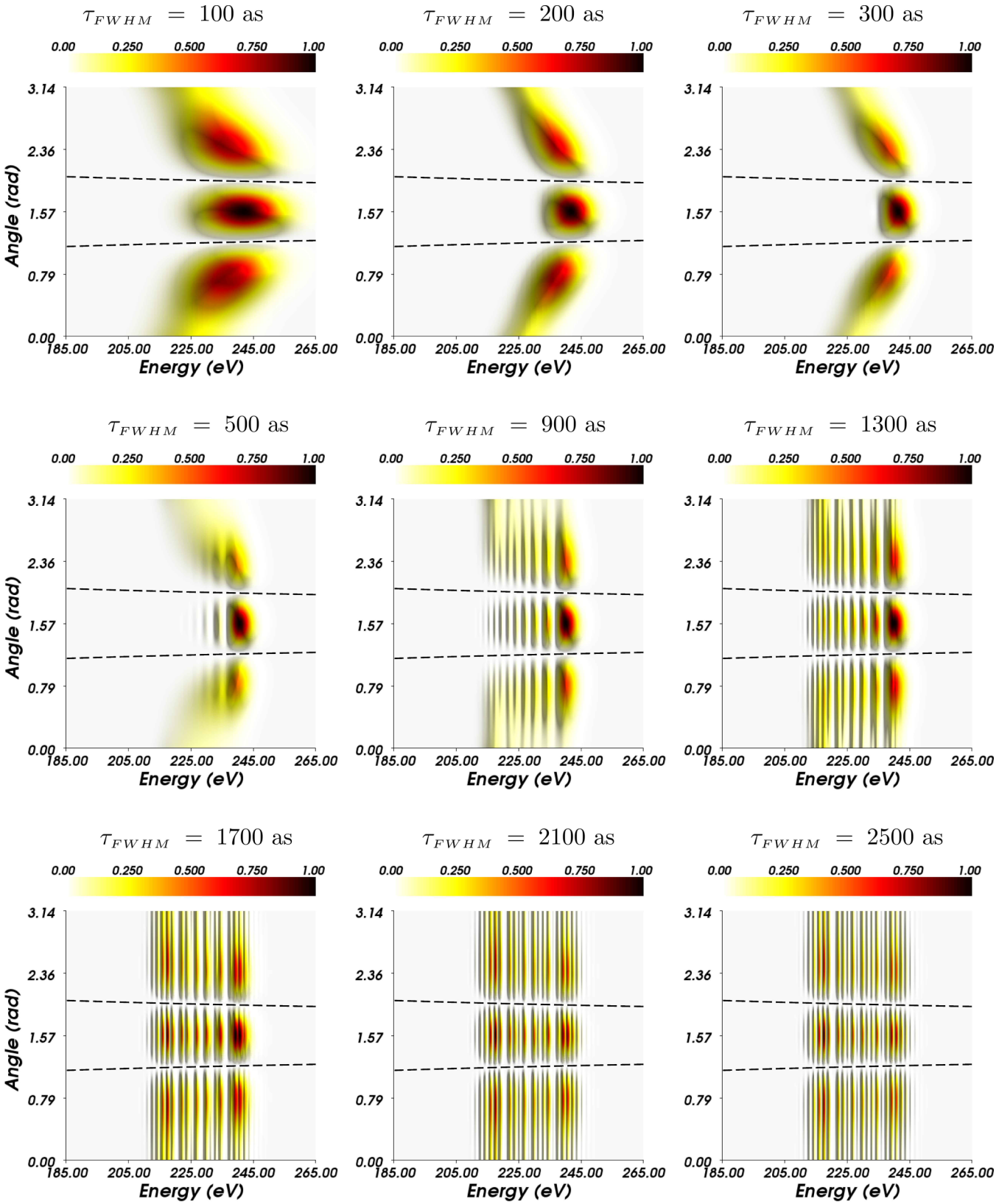

FIG. 9. (Color online) Photoelectron spectra for fixed in space H_2^+ at $R = 2$ a.u. The SATP and the assistant NIR are both circularly polarized. Several pulse durations are considered. The rest of the parameters are the same as in Fig. 3(f).

single XUV pulse analyzed before, the precise knowledge of the delay between the XUV pulse and the NIR may become important to clearly characterize sidebands.

D. ATPT and NIR circularly polarized

Let us consider now ATPT and NIR fields both with the same right circular polarization, in which one component of

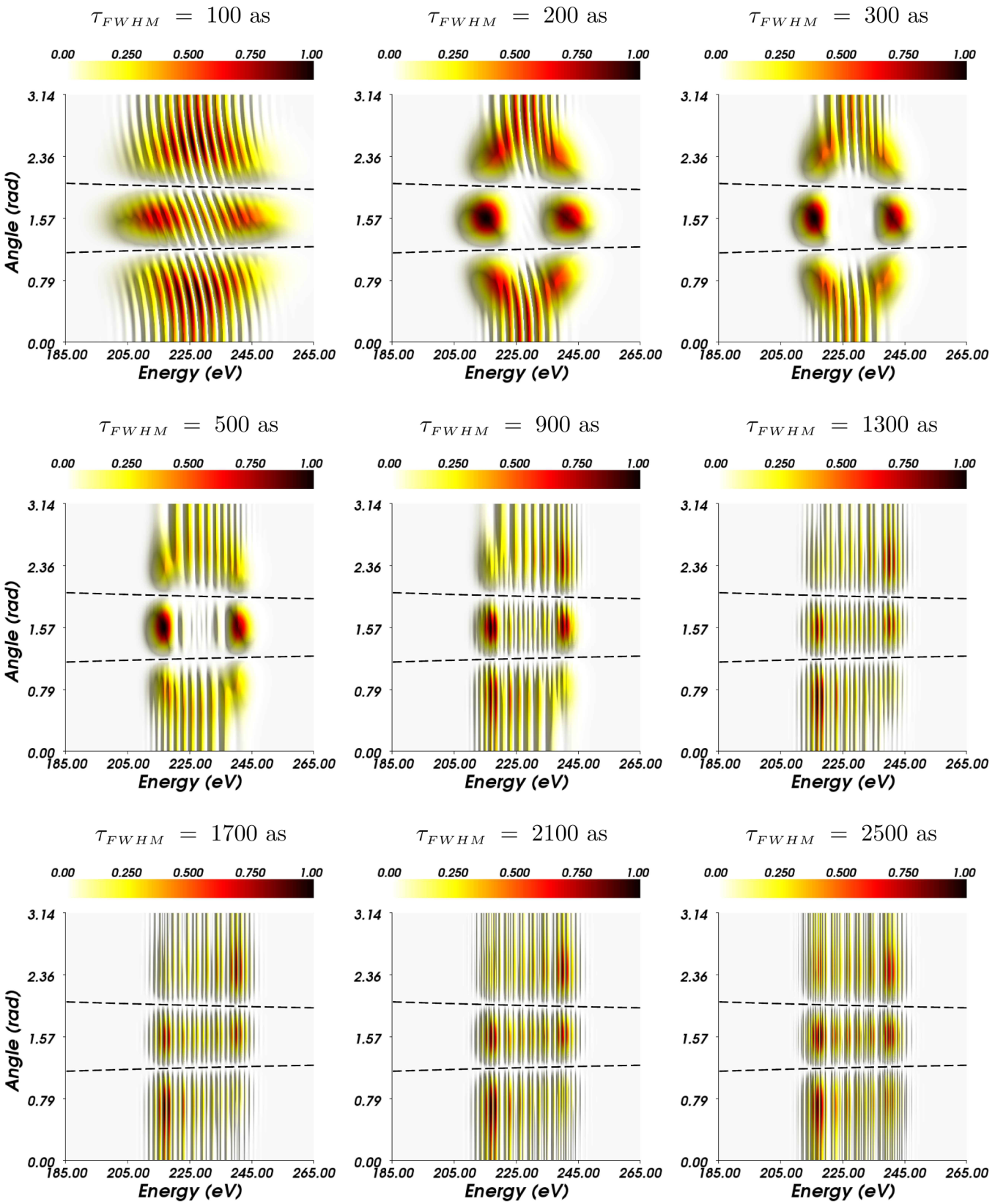

FIG. 10. (Color online) Same as Fig. 9 but for ionization with an ATPT composed by a pulse and a half NIR period delayed replica.

the electric field is parallel and the other one perpendicular to the internuclear separation vector **R**. Although not shown here, the energy-delay photoelectron spectra for different pulse durations in the PDG+ are similar to those for the linear polarization case already shown in Figs. 7 and 8. Instead of them, we present angle-energy photoelectron spectra as they are instructive in order to visualize the emergence of new structures as the pulse duration increases.

In Fig. 9, we show the angle-energy photoelectron spectra for different pulse durations of the SATP. In this case, the delay of the pulse with respect to the NIR is fixed at $t_0 = 0$. By increasing the pulse duration, more sidebands appear as a result of the increase in quantum paths available to reach the same final state. The two angular values where the signal vanishes, almost symmetric with respect to $\theta_e = \pi/2$, are the same as those for which the monochromatic PADs for circular polarization in Fig. 1 vanish. In the plane-wave model of Walter and Briggs [37], PADs follow an angular distribution proportional to $\cos^2(\mathbf{p}\cdot\mathbf{R}/2)$, where the ejection angles at which this expression is zero are shown in Fig. 9 with dashed black lines.

As before, the value $\tau_{\mathrm{FWHM}} = 500$, as seems to be the boundary between the streakinglike behavior and the sideband formation.

If the ATPT is composed by two pulses, then some interesting features arise in Fig. 10. For every pulse duration, photoelectrons ejected in the direction parallel to the molecular internuclear axis are modulated by interference patterns. On the other hand, for ejection in the perpendicular direction to the molecular orientation, interference patterns are present only for small or large durations. No interferences are produced for intermediate τ_{FWHM} values as observed in the case of linear polarization. It is worth pointing out that the delay used in Fig. 10 has the property of separating the perpendicular emission peaks as much as possible. Then, the presence of interferences in the perpendicular emission direction may be modified if other delays are considered.

IV. CONCLUSIONS

We have shown that our simple model is able to describe the main physical features of the photoelectron spectra for H_2^+ molecules in several situations. We have also addressed some issues related to approximations of extended use as SFA, showing some consequences of its use particularly for circular polarization XUV pulses where Coulomb interactions play a major qualitative role. Besides, a quantitative agreement can be achieved for the relative torsion in the monochromatic circular polarization case if the use of peaking approximation is omitted. In general, a qualitative agreement is obtained between the predictions of our simple model and the more elaborate *ab initio* results.

Moreover, we have analyzed the physical origin of PADs asymmetries in laser-assisted photoionization in the streaking regime showing that satellite interferences are responsible for them in a quantum mechanical sense. We have also introduced a fitting procedure that allows the recovery of physically important parameters of the reactions when an ATPT is considered as ionizing signal, in which the individual pulse duration has a second-order importance. We have also analyzed the conditions under which previous interference effects predicted for monochromatic pulses could be enhanced and/or diminished leading to a directional selectivity of the photoelectron emission.

In addition, we have examined the individual pulse duration influence on the photoelectron spectrum for SATPs and ATPTs with linear and circular polarizations. For all the cases analyzed, an individual pulse duration of ∼500 as seems to be an upper boundary for the streaking regime when the NIR has a wavelength of 800 nm. Also, when an ATPT with individual pulse durations similar to the NIR period is considered, a rather small spectrum dependence with the delay is found, indicating that the knowledge of the delay between the ATPT and the NIR might be necessary to properly characterize the sidebands.

These results are encouraging as our calculations may be extended without great effort to more complex diatomic molecules where *ab initio* calculations are computationally very CPU-time consuming or even prohibitive. Work in this direction is in progress.

ACKNOWLEDGMENTS

Authors acknowledge financial support from the Agencia Nacional de Promoción Científica y Tecnológica (PICT No. 2145), and the Consejo Nacional de Investigaciones Científica y Técnicas de la República Argentina (PIP No. 11220090101026).

APPENDIX

1. Monochromatic transition matrix elements

We summarize the basic steps to obtain analytical expressions for the monochromatic transition matrix elements. Replacing Eqs. (6) and (8) into Eq. (15) and performing an expansion of the integral as a sum of integrals over each molecular center, $M_{\mathrm{ph}}(\mathbf{p})$ may be written as

$$M_{\mathrm{ph}}(\mathbf{p}) = M_{\mathrm{ph}}^{(1)}(\mathbf{p}) + M_{\mathrm{ph}}^{(2)}(\mathbf{p}). \tag{A1}$$

To obtain $M_{\mathrm{ph}}^{(1,2)}(\mathbf{p})$, we employ the Coulomb continuum (CC) model [25,26] in which the expression

$$\begin{aligned} M_{\mathrm{ph}}^{(1,2)}(\mathbf{p}) = & -i(2\pi)^{-3/2}(N_p^*)^2 e^{\pm i\mathbf{p}\cdot\mathbf{R}/2} \\ & \times \int d^3r_{1,2} e^{-i\mathbf{p}\cdot\mathbf{r}_{1,2}} G^*(\mathbf{r}_{1,2}) G^*(\mathbf{r}_{1,2} \mp \mathbf{R}) \\ & \times \mathbf{\Pi}(\phi)\cdot\nabla_{r_{1,2}} \sum_j c_j^{(1,2)} \phi_j(\mathbf{r}_{1,2}) \end{aligned} \tag{A2}$$

is approximated by

$$\begin{aligned} M_{\mathrm{ph}}^{(1,2)}(\mathbf{p}) = & -i(2\pi)^{-3/2}(N_p^*)^2 e^{\pm i\mathbf{p}\cdot\mathbf{R}/2} G^*(\mp\mathbf{R}) \\ & \times \int d^3r_{1,2} e^{-i\mathbf{p}\cdot\mathbf{r}_{1,2}} G^*(\mathbf{r}_{1,2}) \mathbf{\Pi}(\phi)\cdot\nabla_{r_{1,2}} \\ & \times \sum_j c_j^{(1,2)} \phi_j(\mathbf{r}_{1,2}), \end{aligned} \tag{A3}$$

provided that the largest contributions to the integral are located around nucleus labeled as 1,2. This approximation, valid when $pR \gg 1$, is usually referred to as the peaking

approximation and leads to the expression

$$M_{\rm ph}(\mathbf{p}) = \chi_1 M_{\rm at}^{(1)} + \chi_2 M_{\rm at}^{(2)}, \tag{A4}$$

where the molecular interference factors denoted by $\chi_{1,2}$ are given by

$$\chi_{1,2} = N_p^* e^{\pm i\mathbf{p}\cdot\mathbf{R}/2} G^*(\mp\mathbf{R}), \tag{A5}$$

including the factored Coulombic term $G^*(\mp\mathbf{R})$ coming from the peaking approximation. The $M_{\rm at}^{(1,2)}$ factors are given by

$$M_{\rm at}^{(1,2)} = -i(2\pi)^{-3/2} N_p^* \int d^3 r_{1,2} e^{-i\mathbf{p}\cdot\mathbf{r}_{1,2}} \times G^*(\mathbf{r}_{1,2})\mathbf{\Pi}(\phi)\cdot\nabla_{r_{1,2}} \sum_j c_j^{(1,2)} \phi_j(\mathbf{r}_{1,2}), \tag{A6}$$

which correspond to the atomic transition matrix amplitudes from the molecular centers 1 and 2, respectively, and they are solved analytically using the Nordsieck's method [38].

2. Taylor expansion of the Volkov phase

We present the approximations performed to obtain Eq. (22). Replacing in Eq. (1) the initial and final wave functions and also the expression for vector potential of the XUV ATPT, we obtain an expression for the transition amplitude. Recalling that in the velocity gauge, time and space integrals are separable, and considering space integrations as performed, then a time integral has to be solved. Now, instead of using the Jacobi-Anger identities, we perform a Taylor expansion of the Volkov phase in Eq. (7), around the arrival time t_k,

$$\theta(t) = \int^t [\mathbf{p} + \mathbf{A}_L(t')]^2 dt' \tag{A7}$$

$$= \theta(t_k) + \theta'(t_k)(t - t_k) + \frac{1}{2}\theta''(t_k)(t - t_k)^2 + \cdots, \tag{A8}$$

and we keep terms up to the second order. Then, the time integral reads

$$I = \sum_k \varsigma_k \int_{-\infty}^{\infty} \exp\left\{ -\frac{(t - t_k)^2}{2\tau^2} + i(I_p - \Omega)t + \frac{i}{2}\left[\theta(t_k) + \theta'(t_k)(t - t_k) + \frac{1}{2}\theta''(t_k)(t - t_k)^2\right]\right\}. \tag{A9}$$

Extracting constant phases and grouping together terms of the same $(t - t_k)$ order, we obtain the following expression:

$$I = \sum_k \varsigma_k e^{i[\frac{\theta(t_k)}{2} + (I_p - \Omega)t_k]} \int_{-\infty}^{\infty} \exp(-\alpha^2\xi^2 + \beta\xi) d\xi, \tag{A10}$$

where

$$\alpha^2 = \left(\frac{1}{2\tau^2} - \frac{i\theta''(t_k)}{4}\right), \tag{A11}$$

$$\beta = i\left(I_p - \Omega + \frac{\theta'(t_k)}{2}\right). \tag{A12}$$

The definite integral in Eq. (A10) has a straightforward solution [39], namely

$$\int_{-\infty}^{\infty} \exp(-\alpha^2\xi^2 + \beta\xi) d\xi = \frac{\sqrt{\pi}}{\alpha} \exp\left(\frac{\beta^2}{4\alpha^2}\right), \tag{A13}$$

with $\mathrm{Re}\alpha^2 > 0$, which can be rewritten as

$$\frac{\sqrt{\pi}\alpha^*}{|\alpha|^2} \exp\left(\frac{\beta^2(\alpha^2)^*}{4|\alpha^2|^2}\right), \tag{A14}$$

with

$$\beta^2 = -\left(\frac{\theta'(t_k)}{2} + I_p - \Omega\right)^2, \tag{A15}$$

$$4|\alpha^2|^2 = \frac{1}{\tau^4} + \frac{\theta''^2(t_k)}{4}, \tag{A16}$$

$$\alpha^* = |\alpha^*| e^{-i\frac{\theta_\alpha}{2}}, \tag{A17}$$

$$\theta_\alpha = -\arctan\left(\frac{\theta''(t_k)\tau^2}{2}\right), \tag{A18}$$

to finally get the expression

$$I \propto \sum_k \varsigma_k \exp\left\{ i\left[\frac{\theta(t_k)}{2}\frac{\left(\frac{\theta'(t_k)}{2} + I_p - \Omega\right)^2}{\frac{4}{\tau^4} + \theta''^2(t_k)} - \theta''(t_k) + (I_p - \Omega)t_k - \frac{\theta_\alpha}{2}\right] - \frac{\left(\frac{\theta'(t_k)}{2} + I_p - \Omega\right)^2}{\frac{2}{\tau^2} + \frac{\theta''^2(t_k)\tau^2}{2}}\right\}, \tag{A19}$$

which is valid when $\theta''^2(t_k)$ is independent of k.

When considering two replicas, with $t_k = \frac{(k+1)\pi}{\omega_0}$, and $k = 0,1$, in the PDG+, i.e., $\theta_e = 0$ or $\mathbf{p} \parallel \mathbf{A}_L$, we have

$$\theta(t_{0,1}) = \frac{E_L^2}{2\omega_0^2} t_{0,1} \mp \frac{2pE_L}{\omega_0^2} + p^2 t_{0,1}, \tag{A20}$$

$$\theta'(t_{0,1}) = p^2, \tag{A21}$$

$$\theta''(t_{0,1}) = \pm 2pE_L. \tag{A22}$$

As $\theta''(t_k)$ does not depend on time, both terms corresponding to $k = 0,1$ in Eq. (A19) may be written as $\mathcal{Z}_2 + \mathcal{Z}_2 e^{i\gamma_2}$, with γ_2 being a phase shift. Under these conditions, we have $|I|^2 \propto (1 + \cos\gamma_2)|\mathcal{Z}_2|^2$, where

$$\gamma_2 = \pi + \frac{2pE_L}{\omega_0^2} + \frac{E_L^2}{4\omega_0^2}\Delta t + \left(\frac{p^2}{2} + I_p - \Omega\right)\Delta t - \arctan(pE_L\tau^2) + pE_L\tau^4 \frac{\left(\frac{p^2}{2} + I_p - \Omega\right)^2}{1 + p^2E_L^2\tau^4}, \tag{A23}$$

with $\Delta t = \pi/\omega_0$, and $|\mathcal{Z}_2|^2$ given by

$$|\mathcal{Z}_2|^2 = \exp\left\{-\tau^2 \frac{\left(\frac{p^2}{2} + I_p - \Omega\right)^2}{1 + p^2E_L^2\tau^4}\right\}. \tag{A24}$$

If only first-order terms in the Taylor expansion are kept, we obtain

$$\gamma_1 = \pi + \frac{2pE_L}{\omega_0^2} + \frac{E_L^2}{4\omega_0^2}\Delta t + \left(\frac{p^2}{2} + I_p - \Omega\right)\Delta t \tag{A25}$$

and

$$|\mathcal{Z}_1|^2 = \exp\left\{-\tau^2\left(\frac{p^2}{2} + I_p - \Omega\right)^2\right\}. \tag{A26}$$

In passing from the second to the first order in the Taylor expansion, a condition of applicability for the latter can be found, namely,

$$pE_L\tau^2 \ll 1. \tag{A27}$$

Interestingly, this relation does not depend on ω_0.

[1] A. H. Zewail, J. Phys. Chem. A **104**, 5660 (2000).
[2] M. Hentschel, R. Kienberger, C. Spielmann, G. A. Reider, N. Milosevic, T. Brabec, P. Corkum, U. Heinzmann, M. Drescher, and F. Krausz, Nature (London) **414**, 509 (2001).
[3] K. Zhao, Q. Zhang, M. Chini, Y. Wu, X. Wang, and Z. Chang, Opt. Lett. **37**, 3891 (2012).
[4] G. L. Yudin, A. D. Bandrauk, and P. B. Corkum, Phys. Rev. Lett. **96**, 063002 (2006).
[5] C. Liu and M. Nisoli, Phys. Rev. A **85**, 053423 (2012).
[6] F. He, C. Ruiz, and A. Becker, Phys. Rev. Lett. **99**, 083002 (2007).
[7] F. He, C. Ruiz, and A. Becker, J. Phys. B: At. Mol. Opt. Phys. **41**, 081003 (2008).
[8] A. Picón, A. Bahabad, H. C. Kapteyn, M. M. Murnane, and A. Becker, Phys. Rev. A **83**, 013414 (2011).
[9] F. Kelkensberg, W. Siu, J. F. Pérez-Torres, F. Morales, G. Gademann, A. Rouzée, P. Johnsson, M. Lucchini, F. Calegari, J. L. Sanz-Vicario, F. Martín, and M. J. J. Vrakking, Phys. Rev. Lett. **107**, 043002 (2011).
[10] G. Laurent, W. Cao, H. Li, Z. Wang, I. Ben-Itzhak, and C. L. Cocke, Phys. Rev. Lett. **109**, 083001 (2012).
[11] M. F. Ciappina, O. A. Fojón, and R. D. Rivarola, J. Phys. B: At., Mol. Opt. Phys. **47**, 042001 (2014).
[12] J. Fernández, O. Fojón, A. Palacios, and F. Martín, Phys. Rev. Lett. **98**, 043005 (2007).
[13] J. Fernández, O. Fojón, and F. Martín, Phys. Rev. A **79**, 023420 (2009).
[14] T. Remetter, P. Johnsson, J. Mauritsson, K. Varjú, Y. Ni, F. Lepine, E. Gustafsson, M. Kling, J. Khan, R. Lopez-Martens, K. J. Schafer, M. J. J. Vrakking, and A. L'Huillier, Nat. Phys. **2**, 323 (2006).
[15] K. Varjú, P. Johnsson, J. Mauritsson, T. Remetter, T. Ruchon, Y. Ni, F. Lépine, M. Kling, J. Khan, K. J. Schafer, M. J. J. Vrakking, and A. L'Huillier, J. Phys. B: At., Mol. Opt. Phys. **39**, 3983 (2006).
[16] F. Krausz and M. Ivanov, Rev. Mod. Phys. **81**, 163 (2009).
[17] J. M. Dahlström, A. L'Huillier, and A. Maquet, J. Phys. B: At., Mol. Opt. Phys. **45**, 183001 (2012).
[18] J. Mauritsson, P. Johnsson, E. Gustafsson, A. L'Huillier, K. J. Schafer, and M. B. Gaarde, Phys. Rev. Lett. **97**, 013001 (2006).
[19] X. He, J. M. Dahlström, R. Rakowski, C. M. Heyl, A. Persson, J. Mauritsson, and A. L'Huillier, Phys. Rev. A **82**, 033410 (2010).
[20] A. Palacios, A. González-Castrillo, and F. Martín, J. Phys. B: At., Mol. Opt. Phys. **47**, 124013 (2014).
[21] S. X. Hu, L. A. Collins, and B. I. Schneider, Phys. Rev. A **80**, 023426 (2009).
[22] J. Fernández, F. L. Yip, T. N. Rescigno, C. W. McCurdy, and F. Martín, Phys. Rev. A **79**, 043409 (2009).
[23] X. Guan, R. C. DuToit, and K. Bartschat, Phys. Rev. A **87**, 053410 (2013).
[24] H. Reiss, Prog. Quantum Electron. **16**, 1 (1992).
[25] G. L. Yudin, S. Chelkowski, and A. D. Bandrauk, J. Phys. B: At., Mol. Opt. Phys. **39**, L17 (2006).
[26] G. L. Yudin, S. Patchkovskii, P. B. Corkum, and A. D. Bandrauk, J. Phys. B: At., Mol. Opt. Phys. **40**, F93 (2007).
[27] G. L. Yudin, S. Patchkovskii, and A. D. Bandrauk, J. Phys. B: At., Mol. Opt. Phys. **41**, 045602 (2008).
[28] O. Fojón, A. Palacios, J. Fernández, R. Rivarola, and F. Martín, Phys. Lett. A **350**, 371 (2006).
[29] C. Neidel, J. Klei, C.-H. Yang, A. Rouzée, M. J. J. Vrakking, K. Klünder, M. Miranda, C. L. Arnold, T. Fordell, A. L'Huillier, M. Gisselbrecht, P. Johnsson, M. P. Dinh, E. Suraud, P.-G. Reinhard, V. Despré, M. A. L. Marques, and F. Lépine, Phys. Rev. Lett. **111**, 033001 (2013).
[30] M. W. Schmidt, K. K. Baldridge, J. A. Boatz, S. T. Elbert, M. S. Gordon, J. H. Jensen, S. Koseki, N. Matsunaga, K. A. Nguyen, S. Su, T. L. Windus, M. Dupuis, and J. A. Montgomery, J. Comput. Chem. **14**, 1347 (1993).
[31] I. Ema, J. M. García de la Vega, G. Ramírez, R. López, J. Fernández Rico, H. Meissner, and J. Paldus, J. Comput. Chem. **24**, 859 (2003).
[32] R. F. Stewart, J. Chem. Phys. **52**, 431 (1970).
[33] R. Della Picca, P. D. Fainstein, M. L. Martiarena, and A. Dubois, Phys. Rev. A **77**, 022702 (2008).
[34] A. K. Kazansky and N. M. Kabachnik, J. Phys. B: At., Mol. Opt. Phys. **40**, 2163 (2007).
[35] A. K. Kazansky and N. M. Kabachnik, J. Phys. B: At., Mol. Opt. Phys. **40**, 3413 (2007).
[36] A. K. Kazansky, I. P. Sazhina, and N. M. Kabachnik, Phys. Rev. A **82**, 033420 (2010).
[37] M. Walter and J. Briggs, J. Phys. B: At., Mol. Opt. Phys. **32**, 2487 (1999).
[38] A. Nordsieck, Phys. Rev. **93**, 785 (1954).
[39] I. S. Gradshteyn and I. M. Ryzhik, *Tables of Integrals, Series, and Products* (Academic Press, New York, 1981).